It's just a phase: high-contrast imaging with patterned liquid-crystal phase plates to facilitate characterization of exoplanets

Doelman, D.S.

Citation

Doelman, D. S. (2021, June 22). *It's just a phase: high-contrast imaging with patterned liquid-crystal phase plates to facilitate characterization of exoplanets*. Retrieved from https://hdl.handle.net/1887/3191978

Cover Page

Universiteit Leiden

The handle https://hdl.handle.net/1887/3191978 holds various files of this Leiden University dissertation.

Author: Doelman, D.S.
Title: It's just a phase: high-contrast imaging with patterned liquid-crystal phase plates to facilitate characterization of exoplanets
Issue Date: 2021-06-22

7 | Simultaneous phase and amplitude aberration sensing with a liquid-crystal vector-Zernike phase mask

Adapted from
D. S. Doelman, F. Fagginger Auer, M. J. Escuti, F. Snik
Published in Optics Letters (2018)

We present an enhanced version of the Zernike wavefront sensor, that simultaneously measures phase and amplitude aberrations. The "vector-Zernike" wavefront sensor consists of a patterned liquid-crystal mask, which imposes $\pm\pi/2$ phase on the point spread function core through the achromatic geometric phase acting with opposite sign on opposite circular polarizations. After splitting circular polarization, the ensuing pupil intensity images are used to reconstruct the phase and the amplitude of the incoming wavefront. We demonstrate reconstruction of the complex wavefront with monochromatic lab measurements and show in simulation the high accuracy and sensitivity over a bandwidth up to 100%.

7.1   Introduction

The introduction of phase-contrast microscopy by Frits Zernike (Zernike, 1934, 1942a,b; Goodman, 1996) was a revolution for the field of biological sciences.While a standard microscope measures intensity variations due to absorption, a phase-contrast microscope measures phase differences from variations in index of refraction by coupling the phase differences into intensity variations with a phase mask inside the microscope. Otherwise unseen transparent structures could now be imaged in great detail. Another application of the phase-contrast method is the Zernike wavefront sensor (ZWFS). The ZWFS has a similar phase mask with a dot that offsets the phase of the core of the point spread function (PSF) by $\pi/2$. The optimal size of the dot is 1.06 λ/D, where D is the pupil diameter and λ the wavelength. The phase-shifted PSF core interferes with the rest of the PSF and phase aberrations are converted to electric field amplitude variations in the subsequent pupil plane (Goodman, 1996; N'Diaye et al., 2013; Guyon, 2005). Thus, a phase-only aberration can be measured directly with one intensity measurement. Extremely sensitive systems like direct-imaging instruments for exoplanet detection use the ZWFS to minimize instrumental aberrations. Non-common path correction with the ZWFS has been successfully demonstrated on-sky (Vigan et al., 2018) and picometer precision has been achieved in the lab for the Wide Field Infrared Survey Telescope (WFIRST) (Shi et al., 2018).

One major advantage of the Zernike wavefront sensor is that it is the most photon-efficient WFS with a sensitivity factor for photon noise of unity (Guyon, 2005; Paterson, 2008). Also, the ZWFS constitutes a simple implementation for any optical system that only requires a focal-plane mask and the ability to image the pupil plane. However, the dynamic range is limited, and the mask applies (wavelength-dependent) scalar phase shifts. In addition, a reference pupil image is needed for static amplitude aberration correction. Therefore, time-variable amplitude aberrations are reconstructed as phase aberrations. Static and dynamic amplitude variations can come from contamination of optics, degradation in optical performance, Fresnel propagation effects, and scintillation. Several systems that measure both amplitude and phase have been proposed, however these systems are complicated (Yamamoto et al., 2015; Cuche et al., 1999) or require diversity in time, like the phase-shifting ZWFS, where a variable-phase Zernike mask is used to reconstruct the complex wavefront with four consecutive measurements (Wallace et al., 2011). In this paper we present a liquid-crystal version of the ZWFS, the "vector-Zernike" wavefront sensor (vZWFS) that enables the simultaneous measurement of both phase and amplitude aberrations. This simple upgrade only requires the replacement of the Zernike mask in addition to splitting circular polarization. The property of optimal photon efficiency is maintained by the vZWFS and a liquid-crystal focal plane mask applies achromatic geometric phase, yielding an improved broadband performance (Bloemhof, 2014).
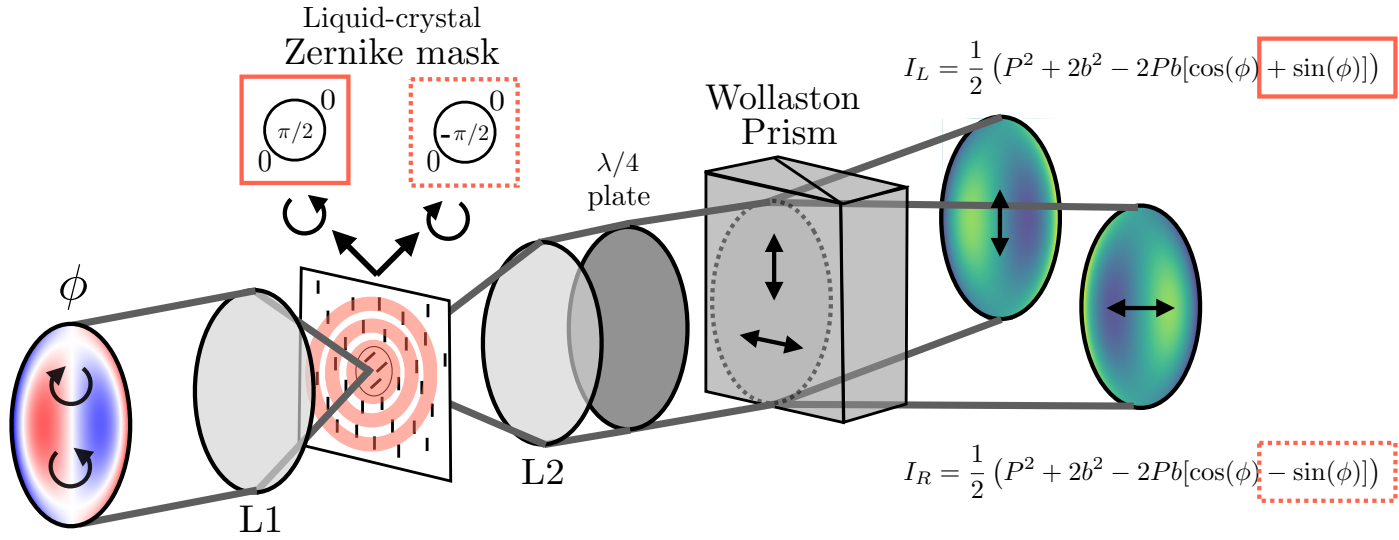
Figure 7.1: Layout of the vector Zernike wavefront sensor. The intensity distribution of the pupils depends on the incoming phase and sign of the polarization state.

7.2   Theory

The geometric phase applied by the mask, $\Delta\theta$, is independent of wavelength and only depends on the fast-axis orientation, α, of the mask and the handedness of the circular polarization state of the incoming light (Escuti et al., 2016)

$$\Delta\theta(x,y) = \pm 2\alpha(x,y). \tag{7.1}$$

Writing complex fast-axis orientation patterns is enabled by liquid-crystal direct-write technology (Miskiewicz & Escuti, 2014) and achromatizing the half-wave retardance is enabled by stacking self-aligning liquid-crystal layers to form a multi-twist retarder (Komanduri et al., 2013). The precise writing capability and broadband performance of this technology has been verified in the lab for other optical elements (Oh & Escuti, 2009; Escuti et al., 2016). A Zernike mask manufactured with liquid-crystal technology simultaneously applies $+\pi/2$ phase to the right-handed circularly polarized fraction of the PSF core and $-\pi/2$ to the left-handed circularly polarized fraction of the PSF core. We split the light with opposite handedness with a quarter-wave plate and a polarizing beam-splitter as shown in Fig. 7.1.

To describe the resulting intensity in the two pupils, we adopt the formalism from N'Diaye et al. (N'Diaye et al., 2013). The electric field at the entrance pupil, Ψ_A, is defined as

$$\Psi_A = Pe^{i\phi} = P_0(1-\epsilon)e^{i\phi}. \tag{7.2}$$

Here P is the normalized amplitude such that P_0 is the pupil function. The variables $\epsilon = \epsilon(u,v)$ and $\phi = \phi(u,v)$ are amplitude aberration and the phase aberration for each position in the pupil plane. Following the derivation of N'Diaye et al. (N'Diaye et al., 2013) and assuming $\theta = \pm\pi/2$, the intensity of the two pupils (I_L and I_R) can be written as

$$I_L = \frac{1}{2}\left(P^2 + 2b^2 - 2Pb[\cos(\phi) + \sin(\phi)]\right) \tag{7.3}$$

$$I_R = \frac{1}{2}\left(P^2 + 2b^2 - 2Pb[\cos(\phi) - \sin(\phi)]\right), \tag{7.4}$$

where b is the convolution of the Fourier transform of the binary Zernike mask and the pupil plane electric field. If the aberrations are small, b can be approximated by b_0, using the pupil function instead of the pupil plane electric field ($\Psi_A = P_0$). Splitting opposite circular polarization states introduces the factor of a half and creates two pupils with different intensities depending on the sign of $\sin(\phi)$. This is used to measure both the amplitude and the phase aberrations in a similar fashion as Wallace et al. (Wallace et al., 2011). They use the sum and the difference of four intensity measurements to directly calculate the amplitude and phase aberration. Here the phase is measured in the same way, only the amplitude is measured as the square root of the pupil intensity. The sum and the difference of the pupil

intensities are given by

$$I_R + I_L = P^2 + 2b^2 - 2Pb\cos(\phi) \tag{7.5}$$

$$I_R - I_L = 2Pb\sin(\phi). \tag{7.6}$$

Using these equations and the identity $\cos^2(\phi) + \sin^2(\phi) = 1$, we solve for the amplitude P and the phase ϕ. The exact reconstruction is given by

$$P = \sqrt{I_R + I_L + \sqrt{4b^2(I_R + I_L) - (I_R - I_L)^2 - 4b^4}} \tag{7.7}$$

$$\phi = \arcsin\left(\frac{I_R - I_L}{2Pb}\right). \tag{7.8}$$

Solving these equations can become numerically unstable for real wavefront sensor applications. Similar to N'Diaye et al. (N'Diaye et al., 2013), we assume that the vector-Zernike wavefront sensor operates in the low-aberration regime, where ϕ dominates the reconstruction. Therefore, $b \approx b_0$ and for the phase reconstruction P = 1. Then we calculate P using the approximated values for ϕ,

$$\phi \approx \frac{(I_R - I_L)}{2b_0} \tag{7.9}$$

$$P \approx \sqrt{I_R + I_L - b_0^2(2 - \cos^2(\phi))} - b_0\cos(\phi). \tag{7.10}$$

Measuring both P and ϕ allows us to estimate the aberrated electric field and approximate b. This process is iterated and converges in the linear regime to the right b, P and ϕ. Note that the reconstruction algorithms do not require many complex calculations such as matrix multiplications to recover the complex wavefront. Therefore the reconstruction is suitable for very fast wavefront reconstruction.

7.3   Simulation

To compare the effect of amplitude aberrations in the reconstruction for both the ZWFS and the vector-ZWFS, we perform numerical simulations of both systems with HCIPy (Por et al., 2018). We start with an unobstructed pupil with both phase and amplitude aberrations as shown in the left column of Fig. 7.2. The input phase aberration has a $\sigma_\phi = 0.22$ rad rms and 1.17 rad peak-to-valley (PtV). The normalized amplitude aberration has a $\sigma_\epsilon = 0.6\%$ rms ($\sigma_I = 1.3\%$) and 3.7% PtV (I: 7.2% PtV), where I is the intensity. We reconstruct the phase for the ZWFS using Eq. 14 in N'Diaye et al. (N'Diaye et al., 2013). For the vector-ZWFS we use three different methods to calculate the phase and the amplitude. The first method (*Linear*), uses modal-based wavefront reconstruction to reconstruct 200 Zernike mode coefficients of the phase and the amplitude uses Eq. 7.10. The second method (2nd *order*) uses Eq. 7.9-7.10 to reconstruct the aberrations directly from the intensity measurements with 5 iterations. The third method (*Exact*) uses Eq. 7.7-7.8 using $b = b_0$ and 5 iterations. We compare the standard deviation of
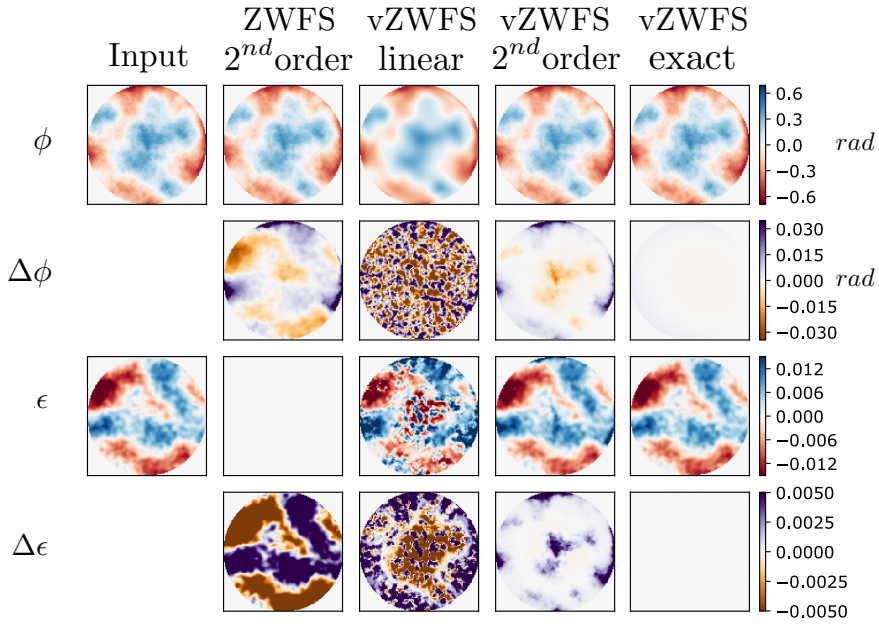
Figure 7.2: Comparison in the simulated reconstruction of both phase and amplitude between the Zernike wavefront sensor (ZWFS) and the vector-ZWFS. The phase aberration is shown in the top row, followed by the residual phase, i.e. the difference between the reconstructed and the input phase. The two bottom rows contain the same with amplitude aberrations. The different columns show the results for different measurement and reconstruction methods.

the residual phase between the ZWFS and the vZWFS and find that the non-linear algorithms of the vZWFS outperform the ZWFS. For the second row in Fig. 7.2, from left to right starting from the input, $\sigma_{\Delta\phi} = [0.221, 0.013, 0.029, 0, 007, 0.001]$ rad rms. The phase reconstruction of the classical ZWFS in the second column of Fig. 7.2 shows that the residual phase aberration in the pupil is caused by the amplitude aberration that it can not directly correct for. This is different from all three vZWFS reconstruction methods, where the residual phase is dominated by the inability to reconstruct high-frequency aberrations with the first 200 Zernike modes (*Linear*), approximations used in the phase calculation (2nd *order*), and the dynamic range of the vZWFS (*Exact*). No significant influence of the amplitude aberration is seen in the residual phase. The amplitude aberration measurements of the vZWFS are dominated by phase estimation errors. The residual amplitude aberrations from left to right, starting from the input, are $\sigma_{\Delta\epsilon} = [1.3, 1.3, 1.4, 0.4, 0.02]\%$ rms.

For practical implementations we look into the influence of imperfect optics shown in Fig. 7.1 and noise on the performance of the vZWFS. Measuring two pupils increases read noise with a factor of 2 and combining the two pupil measurements suffers from flat-fielding effects. In addition, the vZWFS setup requires the use of a liquid-crystal Zernike mask, a quarter-wave plate (QWP) and a polarizing beam splitter (PBS). The vector-Zernike mask has an efficiency (the amount of light that acquires the geometrical phase) that depends on the retardance of the liquid-crystal film (Komanduri et al., 2013). When the phase mask has an offset of the half-wave retardance, $\Delta\delta_{HW}$, the incoming unpolarized light that does not acquire the phase is split by the PBS and adds a background proportional to the pupil intensity. Similar contaminations happen with retardance deviations of the QWP and the rotation of the PBS. The consequent left pupil intensity distributions (identical to the right pupil) from an imperfect HWP, QWP and PBS respectively are given by

$$I_{L,\Delta 1} = I_L \cos^2(\frac{1}{2}\Delta\delta_{HW}) + \frac{1}{2}P^2 \sin^2(\frac{1}{2}\Delta\delta_{HW}), \qquad (7.11)$$

$$I_{L,\Delta 2} = I_L \cos^2(\frac{1}{2}\Delta\delta_{QW}) + \frac{1}{2}(I_L + I_R)\sin^2(\frac{1}{2}\Delta\delta_{QW}), \qquad (7.12)$$

$$I_{L,\Delta 3} = I_L \cos^2(\Delta\theta) + I_R \sin^2(\Delta\theta). \qquad (7.13)$$

To first order, the difference of the pupil intensities is most affected by the extra terms. All terms proportional to $\sin^2()$ drop out and the difference now is proportional to a $\cos^2()$ term that reduces the response. The reduced response can be corrected with a gain factor from calibration. The sum of the pupil intensities is only affected by the deviation from half-wave retardance of the vector-Zernike mask, all other terms sum to the total intensity $I_L + I_R$. The chromatic retardance can be controlled with liquid-crystal technology such that $\Delta\delta_{HW} < 16°$ (Komanduri et al., 2013) for a large bandwidth, i.e. the leakage is $< 2\%$ of the intensity.
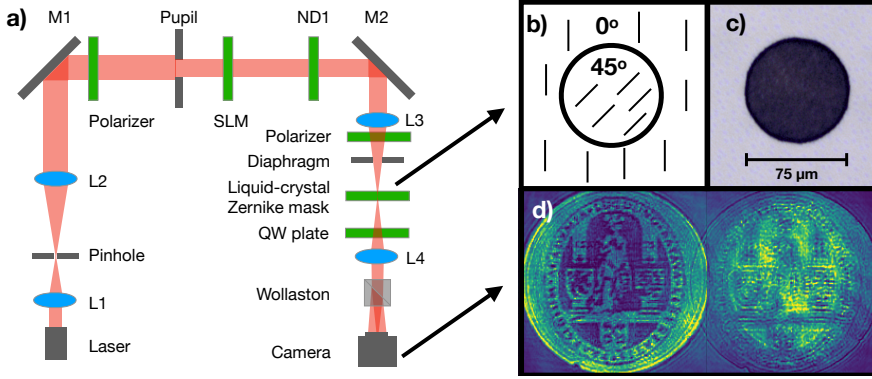
Figure 7.3: **a)** Layout of the vector-Zernike wavefront sensor setup. We generate a clean beam with a laser (633 nm) and a pinhole. A spatial light modulator is operated in phase-mostly configuration with two polarizers and is used to generate phase aberrations with a complicated pattern (i.e. the Leiden University logo). This configuration also generates some amplitude aberrations. The light is focused on the vector-Zernike mask with a spot diameter of 75 μm, corresponding to $\sim$ $1\lambda/D$. The liquid-crystal orientation is shown in panel **b)** and a parallel polarizer microscopic image is shown in panel **c)**. The detector image with aberrated pupils is shown panel **d)**, showing some pupil overlap because of the splitting angle of the Wollaston.

7.4   Lab results

As a proof of principle, we demonstrate the vector-Zernike wavefront sensor with a monochromatic setup. We manufactured a liquid-crystal vector-Zernike mask with a central spot diameter of 75μm, printed on a glass substrate (1 inch diameter, 1 mm thick, BK7) with an effective pixel size of 2 μm. The retardance was tuned to be $\lambda/2$ at 633 nm with a single liquid-crystal layer. Fig. 7.3 b) shows the fabricated mask that does not contain any significant defects. The edges have a smooth fast-axis transition region from 0° to 45° of 2-3 micron. This can be mitigated by modifying b for calculating P and ϕ, although the effect is negligible. We test the performance of the vector-Zernike using the setup shown in panel a) of Fig. 7.3. We use a LC2002 transmissive spatial light modulator (SLM) from HoloEye in phase-mostly configuration to generate phase aberrations. In this configuration the rotation of the liquid-crystals in combination with the polarizers also generates amplitude aberrations. The Wollaston prism is a WPQ10 prism from Thorlabs and the QWP is an achromat (AQWP05M-600) from Thorlabs. Panel d) in Fig. 7.3 shows a raw image after applying a binary logo of Leiden University on the SLM. For the characterization of phase and amplitude reconstruction we minimize the influence of the system by combining measurements with positive and negative phase applied by the SLM. We mean-combine them to remove the
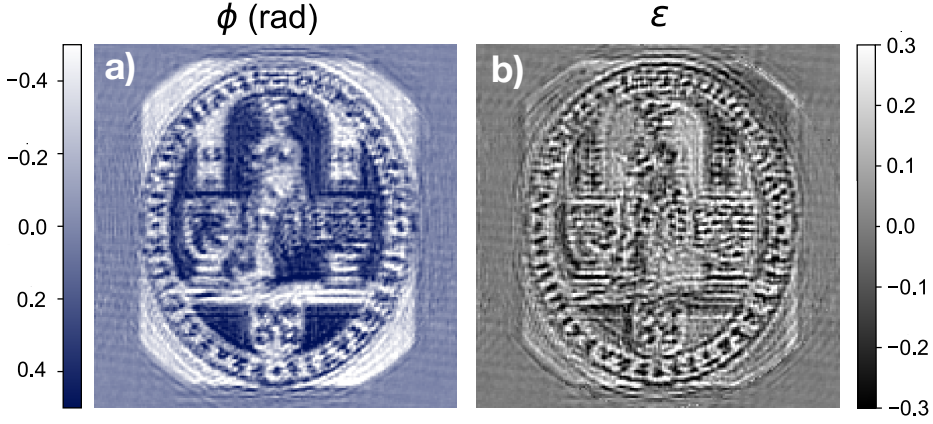
Figure 7.4: **a)** Reconstructed phase and **b)** reconstructed amplitude aberration using the vector-Zernike wavefront sensor.

non-SLM aberrations and we bin the image per 2 pixels to increase the signal to noise. We also take images without any phase applied on the SLM and use them for calculating the pupil intensity necessary for normalizing the aberrated images without taking out the vector-Zernike mask. Note that taking the average pupil intensity does not normalize the measurements correctly. Assuming $\phi \ll 1$, we solve Eq. 7.5 with $\cos \phi = 1$, such that P is given by

$$P = \sqrt{(I_L + I_R)/(1 + 2b_0^2/P^2 - 2b_0/P)}. \tag{7.14}$$

When $\epsilon \ll 1$, the normalized quantity $b_0/P \approx b_0/P_0$ and we calculate the normalization factor of the pupil images by estimating b_0 and averaging P over the pupil. We calculate the phase and amplitude from the two aberrated normalized pupils with Eqs. 7.9 - 7.10. Both measurements contain Fresnel diffraction effects from the out-of-plane diaphragm used as field stop. Determining the accuracy of the reconstruction is not possible as we do not know the details of this SLM.

7.5 Chromaticity of the vZWFS

One additional advantage of the liquid-crystal vector-Zernike wavefront sensor is that the phase is applied achromatically cf. Eq. 7.1. The classical ZWFS has decreased performance with increasing spectral bandwidth because of the chromatic phase of the focal plane mask in combination with the PSF scaling with wavelength. Both contribute to a suboptimal coupling of phase aberrations in the system to intensity variations in the ZWFS pupil plane (N'Diaye et al., 2013). We study the effect of the achromatic phase and the different reconstruction on the broadband performance of the vZWFS in simulation, taking into account the
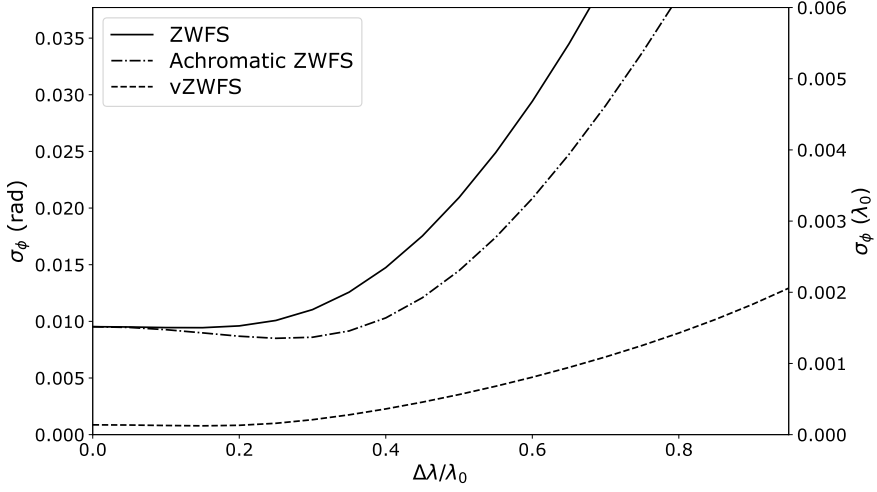
Figure 7.5: Residual wavefront aberrations as function of bandwidth for both the classical ZWFS and the vZWFS. The "achromatic ZWFS" uses the classical ZWFS reconstruction on one pupil of the vZWFS.

spatial scaling of the PSF with wavelength. For this, we exclude amplitude aberrations. Fig. 7.5 shows the results for both wavefront sensors up to 100% bandwidth, i.e. $\lambda/\lambda_0 = 0.5 - 1.5$. We assume a $1/\lambda$ scaling for the applied phase of the classical Zernike mask centered around λ_0 and b_0 is calculated at λ_0 as well. We investigate the influence of only the achromatic phase by using the classical ZWFS reconstruction on one of the vZWFS pupils, the "achromatic ZWFS". Note that all other chromatic effects, including leakage from polarization optics, are not taken into account in this simulation. Fig. 7.5 shows that the vZWFS with exact reconstruction outperforms the classical ZWFS for all bandwidths. Similarly, the classical reconstruction with the "achromatic ZWFS" improves the broadband performance, in agreement with Bloemhof (Bloemhof, 2014). The gain of using only achromatic phase is not as significant as the gain from the reconstruction using two pupils. The reason is that the classical ZWFS uses a second-order reconstruction that is sensitive to the chromatic b, while the vZWFS allows for an exact solution. Iterating the estimate of b with the updated phase and amplitude estimates removes the bias introduced by the chromaticity. Overall we show in simulation that the vZWFS can handle an increased bandwidth, up to 100%.

7.6   Conclusion

We conclude that the liquid-crystal vector Zernike wavefront sensor (vZWFS) is a simple yet powerful upgrade of the classical ZWFS. We show that both amplitude and phase aberrations can be measured simultaneously by replacing the Zernike mask with a liquid-crystal version and splitting circular polarizations in two pupils. We demonstrate both in simulations and with a monochromatic lab setup an improved reconstruction of the complex wavefront with the vZWFS. Like the ZWFS, the vZWFS is the most photon-efficient wavefront sensor (Guyon, 2005) and we demonstrate with simulations the accurate reconstruction for bandwidths up to 100%. For direct-imaging of exoplanets the vZWFS can be installed a parallel WFS beam path, alternated with a coronagraph (Vigan et al., 2018), or built into a coronagraph (Shi et al., 2018).

Bibliography

Bloemhof, E. 2014, Proc. SPIE, 8999, 89991k

Cuche, E., Marquet, P., & Depeursinge, C. 1999, Applied optics, 38, 6994

Escuti, M. J., Kim, J., & Kudenov, M. W. 2016, Optics and Photonics News, 27, 22

Goodman, J. 1996, Introduction to Fourier Optics, Electrical Engineering Series (McGraw-Hill). https://books.google.nl/books?id=jMcsmwEACAAJ

Guyon, O. 2005, The Astrophysical Journal, 629, 592

Komanduri, R. K., Lawler, K. F., & Escuti, M. J. 2013, Optics Express, 21, 404

Miskiewicz, M. N., & Escuti, M. J. 2014, Optics Express, 22, 12691

N'Diaye, M., Dohlen, K., Fusco, T., & Paul, B. 2013, Astronomy & Astrophysics, 555, A94

Oh, C., & Escuti, M. J. 2009, Optics Letters, 34, 3637

Paterson, C. 2008, Journal of Physics: Conf. Series., 139, 012021

Por, E. H., Haffert, S. Y., Radhakrishnan, V. M., et al. 2018, Proc. SPIE, 10703, 1070342

Shi, F., Seo, B.-J., Cady, E., et al. 2018, Proc. SPIE, 10698, 106982O

Vigan, A., N'Diaye, M., Dohlen, K., et al. 2018, arXiv preprint arXiv:1806.06158

Wallace, J. K., Rao, S., Jensen-Clem, R. M., & Serabyn, G. 2011, Proc. SPIE, 8126, 81260F, doi: 10.1117/12.892843

Yamamoto, K., Matsuo, T., Imada, H., & Kino, M. 2015, Applied optics, 54, 7895

Zernike, F. 1934, Monthly Notices of the Royal Astronomical Society, 94, 377

—. 1942a, Physica, 9, 686

—. 1942b, Physica, 9, 974